

Crystallization processes in the phase change material $\text{Ge}_2\text{Sb}_2\text{Te}_5$: Unbiased density functional/molecular dynamics simulations

J. Kalikka,^{1,2} J. Akola,^{2,3} and R. O. Jones^{4,*}¹*Singapore University of Technology and Design, 8 Somapah Road, Singapore 487372*²*Department of Physics, Tampere University of Technology, P.O. Box 692, FI-33101 Tampere, Finland*³*COMP Centre of Excellence, Department of Applied Physics, Aalto University, FI-00076 Aalto, Finland*⁴*Peter Grünberg Institut PGI-1 and JARA/HPC, Forschungszentrum Jülich, D-52425 Jülich, Germany*

(Received 12 July 2016; revised manuscript received 22 September 2016; published 17 October 2016)

Three extensive density functional/molecular dynamics simulations of the crystallization of amorphous $\text{Ge}_2\text{Sb}_2\text{Te}_5$ (460 atoms) [Phys. Rev. B **90**, 184109 (2014)] have been completed with simulation times of up to 8.2 ns. Together with the results of earlier simulations with and without a crystallite seed, the results clarify essential features of a complicated process. They emphasize, in particular, the stochastic nature of crystallization, the effect of bond orientations and percolation, and the importance of extended simulations of sufficiently large samples. This is particularly evident in describing the role of crystallites that can merge to form larger units or hinder complete crystallization by the formation of grain boundaries. The total pair distribution functions for the final structures are compared with available neutron and x-ray diffraction data.

DOI: [10.1103/PhysRevB.94.134105](https://doi.org/10.1103/PhysRevB.94.134105)

I. INTRODUCTION

Rewritable optical storage media such as the digital versatile disk (DVD-RW) and the Blu-ray Disc are based on the extremely rapid and reversible crystallization of amorphous “bits” in thin polycrystalline layers of particular chalcogenide alloys. Some common examples of such “phase change” (PC) materials are $(\text{GeTe})_{1-x}(\text{Sb}_2\text{Te}_3)_x$ pseudobinary alloys [$\text{Ge}_2\text{Sb}_2\text{Te}_5$ (GST), $x = 1/3$, is a much studied prototype] and doped alloys of Sb and Te near the eutectic composition $\text{Sb}_{70}\text{Te}_{30}$. The rate-limiting process in the write/erase cycle is the recrystallization of the amorphous bit, and this has led to a great deal of interest in the details of the crystallization process and in the amorphous and liquid structures [1–5].

Our work on PC materials has used combined density functional [6] (DF)/molecular dynamics (MD) calculations and focused first on the structure of amorphous (*a*-)GST and other members of the Ge/Sb/Te family [7–9], which identified “*ABAB* squares” (*A*: Ge or Sb; *B*: Te) as a crucial motif in this family. This pattern also occurs in the metastable (rocksalt) structure of GST [10,11], so that the reorientation of disordered *ABAB* squares, supported by the presence of cavities, is a possible explanation of their rapid crystallization. The first simulations of this process supported this picture [12]. Crystallization occurs in these materials on a time scale of nanoseconds. Although such times are accessible to DF/MD calculations, it is essential to use simulation samples with several hundred atoms, and the requirements of such computations are extremely demanding. Our initial studies covered a 460-atom sample of *a*-GST at 500, 600, and 700 K [13], where we used a fixed crystalline seed (58 atoms, 6 vacancies) and observed crystallization at 600 and 700 K.

Our most extensive simulations of crystallization of 460-atom samples of GST extended up to 4 ns at 600 K *without* structural constraints [14]. A sample with a previous history

of order (*run0*) crystallized in 1.2 ns, and the process was discussed in detail in Ref. [14]. Crystallization was accompanied by an increase in the number of *ABAB* squares, percolation of crystalline units, and the occurrence of low-frequency localized modes. The process was incomplete in three samples *without* a history of order, even after 4 ns. These simulations are continued to completion here, which required more than 8 ns in one case. The time step (3.0236 fs) means that *each* simulation of this scale requires of the order of 2 million self-consistent DF calculations of forces and energies in a 460-atom sample, which is a major numerical undertaking by any measure. The results emphasize differences between crystallization of samples with and without a history of order, and the stochastic nature of crystallization is underscored by the difficulty in predicting the course of individual, incomplete simulations. Most methods we use for calculation and data analysis have been described in detail previously [13,14], and we restrict our description in Sec. II to essential points and new features. The results are presented and discussed in Secs. III and IV, respectively, and our concluding remarks follow (Sec. V).

II. METHODS OF CALCULATION AND ANALYSIS

NVT simulations (constant particle number *N*, volume *V*, and temperature *T*) of *a*-GST (460 atoms, 600 K, time step 3.0236 fs) were performed using the CPMD program [15] with Born-Oppenheimer MD in a cubic simulation cell. The kinetic energy cutoff of the plane-wave basis, the approximation for the exchange-correlation energy, the pseudopotentials, and the method of temperature control are described elsewhere [14]. The original DF/MD structure of *a*-GST [7], which agreed well with experimental results [9] (see also Sec. IV), was again taken as the starting structure.

Our simulations of crystallization in PC materials differ from others in that the density is changed in steps from the amorphous (0.0308 atoms/Å³) to the crystalline value (0.0330 atoms/Å³) by changing the size of the cell to reflect

*r.jones@fz-juelich.de

the fraction of crystalline atoms in the sample. These are identified by using the order parameter defined by Steinhardt, Nelson, and Ronchetti [16]. In practice, we have changed the density by the corresponding amount when the fraction of crystalline atoms passes 0.2, 0.4, 0.6, etc. In addition, the cell size was changed in *run0* at 0.3, 0.5, and 0.7 during the rapid crystallization phase. The steplike density changes increase the pressure of the system by ~ 0.2 GPa, most of which relaxes before the next change. The pressure does not necessarily return to the original value, however, and there is a modest increase (up to 1 GPa) during a full simulation. All runs start at 2.2–2.3 GPa and end at 3.2, 2.7, 3.2, and 2.7 GPa for *run0* – 3, respectively. The highest pressure observed is ~ 3.5 GPa in *run0* immediately after the last density change, before relaxing to 3.2 GPa at the end of the simulation. The pressures in the cell reflect the use of the PBEsol functional, which generally overestimates bond lengths in these systems, and the elevated temperature of the simulation. Nevertheless, this strategy has advantages over choosing a fixed, possibly arbitrary density for the entire simulation.

The MD trajectories provide the coordinates and velocities of all particles throughout the simulations, enabling us to calculate pair distribution functions (PDFs) of all atom types and cavities, average coordination numbers, (partial) structure factors, percolation of crystalline structural units as a function of time, mean square displacements (MSD) of the atoms, the speed of crystallization, and the vibration frequency distribution (power spectrum). Full details are provided in Ref. [14]. Cavities (vacancies, voids) are defined as in our previous work [7,8,13] and calculated using the PYMOLDYN program [17]. We introduce here a method of analyzing the relationship between cavity volumes and the local atomic environment.

III. RESULTS

The starting configurations of the three simulations were obtained by different paths from the structure of *a*-GST determined in Ref. [7]. These three simulations had no history of order and differed only in their initial velocity distributions: *run1* used the *a*-GST structure of Ref. [7] with the velocity distributions generated at 600 K, the starting structure of *run2* was found after an additional 500 MD steps using velocity scaling, and *run3* was derived from the structure of *run2* with 500 further MD steps with velocity scaling at 600 K.

A. Total energy, crystallinity, percolation

Order was much slower than in the sample with a history of order (*run0*) and required up to 8.2 ns: the largest crystalline clusters were 270 (59%) atoms in *run1*, over 415 (90%) atoms in *run2*, and 355 (77%) atoms in *run3*. Percolation occurred in all cases: *run1* percolates from 1 ns with the largest fraction of crystalline atoms, *run2* begins percolating between 2 and 3 ns, and *run3* percolates after 3 ns. The onset of nuclear growth appears to follow the first signs of percolation and is preceded by a phase of subcritical nuclei with 10–50 atoms. The change in the total energy [Fig. 1(f)] shows that structural relaxation occurs from the outset. The final total energy in *run2* and *run3*, relative to the amorphous state, is -80 meV/at, and it is slightly higher (-75 meV/at) in

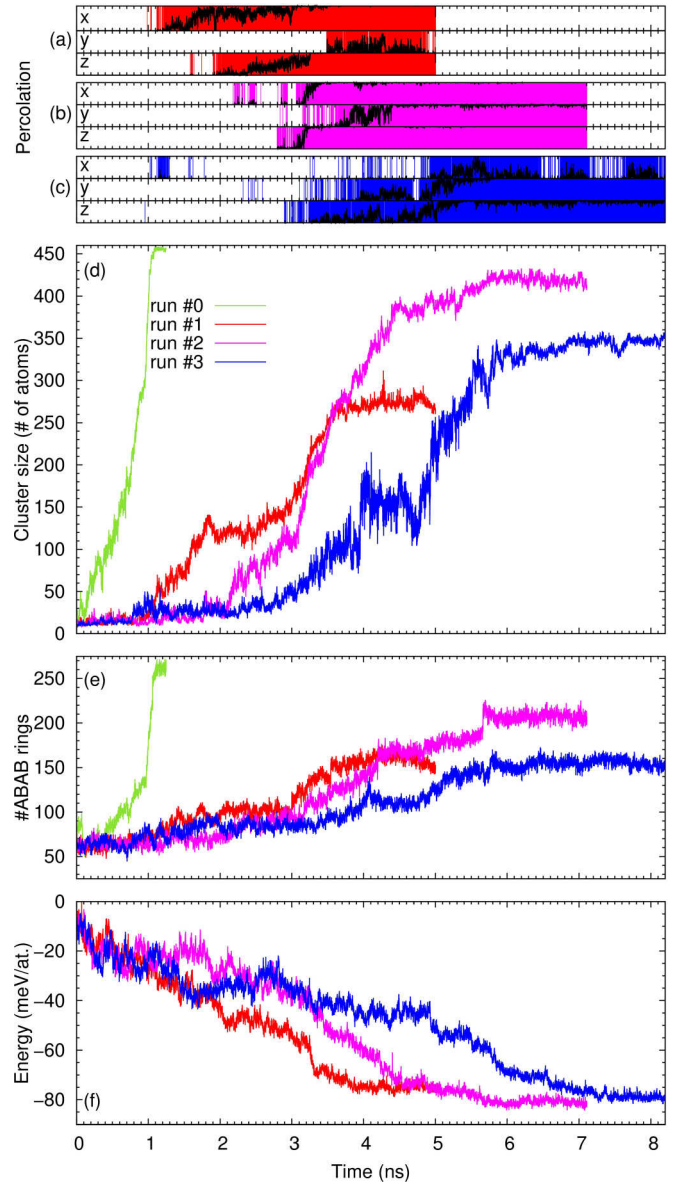


FIG. 1. Three simulations (*run1* – *run3*) starting from the amorphous structure of Ref. [7]. (a)–(c) Percolation in the *x*, *y*, and *z* directions. Black: fraction of percolating frames in 1 ps windows, colored background: percolating frames. (d) Size of the largest cluster, (e) number of *ABAB* squares, including *run0*, and (f) total energy (normalized for box size). Green: *run0*, red: *run1*, purple: *run2*, blue: *run3*.

run1, where there are two unaligned clusters. The final value for the initially amorphous sample with a history of order (*run0*) is -100 meV/at [14], and that for the simulation with a crystalline seed is -110 meV/at [13]. The correlation between order and low total energy is clear.

The cluster sizes and shapes vary greatly, and nuclear growth is evident in *run1* already after 1 ns, before which the unstable nuclei of 40–60 atoms are far from spherical or cubic. Fused *ABAB* squares and cubes are present, with interconnecting bonds. After percolation (1 ns), a crystallite grows to extend over the whole simulation box in one direction until it collides (after 2 ns) with another nucleus with a

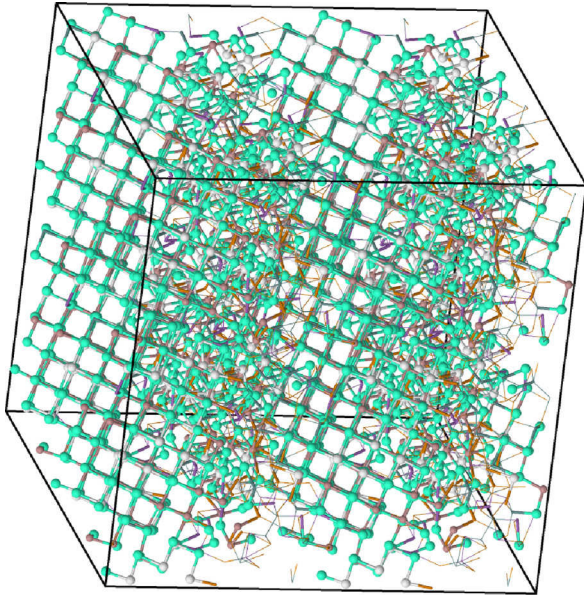


FIG. 2. Optimized structure of *run1* (eight replicas). Crystalline atoms ball-and-stick (Ge: brown, Sb: gray, Te: cyan), amorphous atoms thin lines (Ge: green, Sb: purple, Te: orange).

different orientation. Crystal growth slows until 3 ns, after which the larger nucleus continues to grow. Finally (after 5 ns), the largest cluster is a continuous crystalline slab occupying approximately one half of the simulation cell and percolating in the x and z directions. The other half is occupied by the second largest cluster, which can be described as a continuous, percolating rod in the z direction with a diameter of about half of the width of the simulation cell. The rest of the cell is occupied by amorphous atoms and small (<30 atoms) crystallites. The final structure of *run1* is shown in Fig. 2 (replicated $2 \times 2 \times 2$ times) from a perspective that shows the crystallinity of the ordered slab, while the rod with another alignment is also visible. A view along the z axis that shows the two crystallites more clearly is given in Fig. SF1 of the supplemental material [18].

The second simulation (*run2*) shows a single dominant nucleus and percolation in all three directions, which is consistent with the rapid crystal growth after 2.5 ns (Fig. 1). The growth slows after 4.5 ns, and the largest cluster approaches 415 atoms after 7 ns. This cluster occupies most of the simulation cell with some tens of amorphous atoms, which are located mainly in a plane in the xz direction. The amorphous atoms are rather sparse (see Fig. 3), and they do not block percolation of the crystalline cluster in the y direction.

Simulation *run3* begins slowly and grows rapidly only after 3 ns. As in the case of *run1*, *run3* has two main clusters between 3 and 6 ns. After 5 ns, the larger cluster grows at the expense of the second, which shrinks to less than 30 atoms after 6 ns. The larger cluster grows rapidly between 3 and 4 ns and again between 5 and 6 ns and comprises ~ 355 atoms at 8.2 ns (see Fig. 4). The cluster is a slab similar to the largest cluster of *run1*, and the alignment is such that the crystallite and its replica are not consistent. This results in a dense amorphous slab that blocks the percolation of the largest cluster in the x direction [Fig. 1(c)].

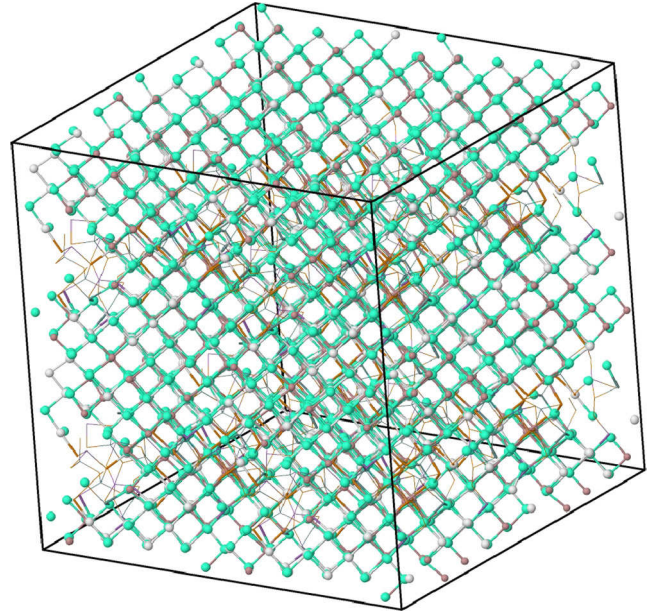


FIG. 3. Optimized structure of *run2* at 7.1 ns (eight replicas). Color code: see Fig. 2.

Simulations *run1* – 3 show plateaus before crystallization, and nuclei grow in directions unrelated to the axes of the simulation box. The slowest evolution is observed for *run3*. Crystallization begins only near 4 ns with two colliding nuclei, although there is occasional percolation and a gradual decrease in total energy beforehand. In *run1* and *run2*, ordering begins after 1 and 2 ns, respectively. The bond directions in simulations *run1* – 3 show isotropic distributions early in the simulations (up to ~ 2 ns), whereas the bond vectors in *run0* tend to lie parallel to the cell axes already during the first 400 ps [14].

The critical size for nucleation is difficult to define, but it is qualitatively different in *run1* – 3. In all three simulations,

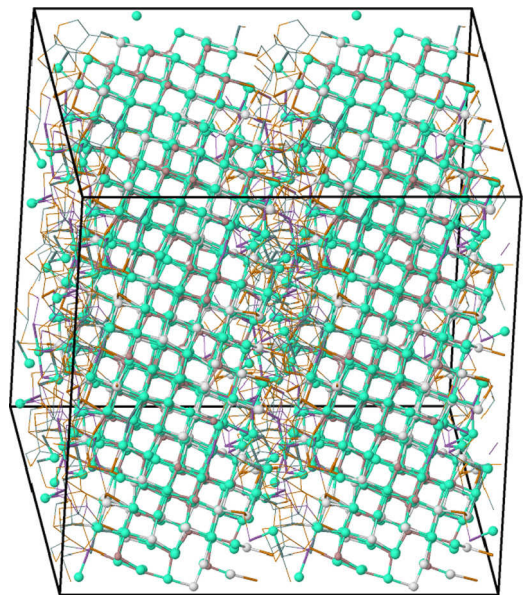


FIG. 4. Optimized structure of *run3* at 8.2 ns (eight replicas). Color code: see Fig. 2.

there are phases (>1 ns) where clusters fluctuate between 10 and 50 atoms. The varying shapes of nuclei include stringlike and branched configurations of crystalline atoms and fused *ABAB* squares percolating throughout the system *before* crystal growth. Such nonspherical cluster shapes reflect the orthogonality of the *p*-type bonds in GST and are not consistent with the assumption of spherical nuclei in classical nucleation (CN) theory. We have noted [14] several differences between the present results and those of larger MD simulations of GeTe using a classical force field [19]. Multiple nuclei found in *run1* and *run3* were also observed below 600 K in GeTe, and the presence of multiple nuclei slows crystallization in all cases. However, the growth of supercritical nuclei is always very rapid (less than 4 ns) in the classical MD simulations of GeTe in this temperature range [19], and subcritical, highly anisotropic nuclei appear not to occur in GeTe.

The speed of crystallization is difficult to determine precisely, but its order of magnitude can be estimated. We focus on the region of rapid change in the number of crystalline atoms that follows subcritical growth [Fig. 1(d)], and we note the time and the cluster size at the beginning and end of this region. From the volume of the cluster, we can then estimate an effective radius and the way it changes with time. This simple analysis leads to crystallization speeds $\sim 0.3\text{--}0.4$ m/s in *run1* – 3, although higher values could occur in larger simulation cells, where the effect of incommensurability of the cell size with the crystal structure would be smaller. The same analysis applied gives a crystallization speed of $\sim 0.7\text{--}0.9$ m/s in *run0*, which differs from the others in both the memory effect and the orientation of the crystallite parallel to the axes of the cell. Density functional simulations of the growth of crystalline nuclei in GST and of the crystallization of planar amorphous-crystalline GST interfaces both led to growth velocities in the range 1 m/s [20]. All these estimates are less than the value found in differential scanning calorimetry (DSC) measurements at 600 K (2.5–3.0 m/s) [21]. Measurements on melt-quenched GST cells give much lower values, the maximum being below 0.1 m/s at 580 K [22].

B. “*ABAB* squares,” wrong bonds

The *ABAB* structural unit (*A*: Ge or Sb; *B*: Te) is an established characteristic of the crystallization process in GST materials [7,12]. As shown in Fig. 1, the increase in the number of such units as the process develops is steady, although less dramatic than in *run0*.

The presence of wrong bonds, particularly Te-Te, in our crystallized samples is striking, and Ge-Ge and Te-Te bonds are also present in simulations performed on GeTe [19]. Due to the partial crystallinity of *run1* – 3, wrong bonds are more abundant in their final structures than in that of *run0*, which crystallized completely. Moreover, the number of wrong bonds does not stabilize to a static value, as in *run0*, because of partial crystallinity. The trends, however, are similar: numbers of homopolar (Ge-Ge, Sb-Sb, and Te-Te) wrong bonds are halved between initial and final structures, except for the number of Ge-Ge bonds in *run2*, which is reduced to around one quarter of the initial value in the final structure. In *run0*, the number of Ge-Sb wrong bonds was reduced to one quarter, in *run1* – 2 to one third, and in *run3* to half of the initial values (see Fig. 5).

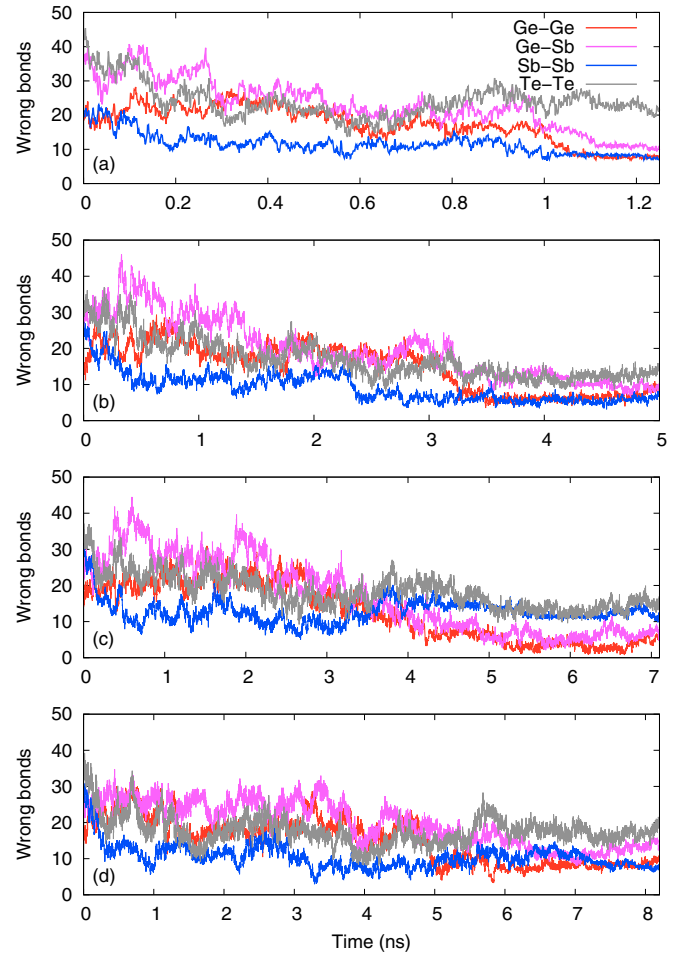


FIG. 5. Wrong bonds of each type in (a) *run0* with memory effect, and (b)–(d) *run1* – 3 without memory effect. Colors: Ge-Ge in red, Ge-Sb in magenta, Sb-Sb in blue, and Te-Te in gray.

C. Cavities

The total cavity volumes of *run1* – 3 (Fig. 6) differ from the run with the ordered history (*run0*), which had the largest total cavity volume, initially $\sim 1800 \text{ \AA}^3$. The others (*run1* – 3) started with $\sim 1300\text{--}1400 \text{ \AA}^3$ of cavities. This is remarkable, since the initial structure of *run0* differed from those of *run1* – 3 only in having an unconstrained seed and a few perturbed neighbors. The smaller total cavity volumes in the final structures of *run1* – 3 ($600\text{--}800 \text{ \AA}^3$) are consistent with partial crystallization, and the difference from *run0* (which ultimately had 900 \AA^3 of cavities) is smallest in *run2*, which is the most crystalline of the three.

The local environment of the cavities was classified into three categories based on the nature of the surrounding atoms. The cavity construction is based on “domains,” which are the parts of the simulation cell farther from any atom than a specified distance (here 2.8 \AA). The closest atom to each domain center is determined, and r_{\min} is defined as its distance from the center. All atoms within a distance $r_{\min} + 0.5 \text{ \AA}$ of the center were defined as “neighboring atoms” of that domain. If all such neighbors were crystalline or amorphous, the cavity was defined as such. The presence of both types meant that the cavity had a “hybrid” environment. In the case of multicavities,

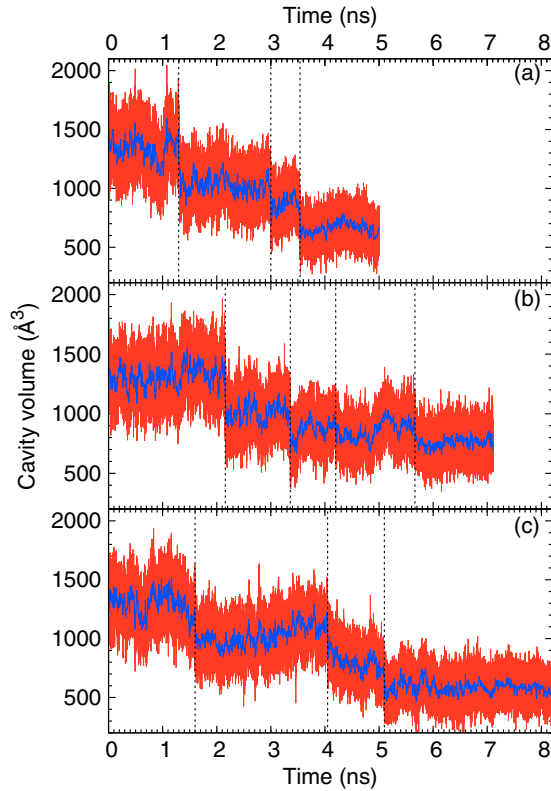


FIG. 6. Variation of total cavity volume in *run1* – 3. Red: raw data; blue: average over 1 ps intervals. Vertical dashed lines show changes in box size.

the atoms neighboring any of the domains were checked and the cavity type was assigned accordingly.

Large fractions of the cavities are in hybrid environments throughout the simulations, indicating that the small crystallites in a mainly amorphous material have many neighboring cavities. In crystalline materials, the amorphous atoms (defects) host a significant fraction of the cavities. As shown in Fig. 7 for the end of *run0*, half of the cavities (by volume) are near defects, and the other half is surrounded by crystalline atoms alone. This applies also to the other simulations as crystallization is approached. This indicates an association between point defects in the crystalline lattice, wrong bonds, and cavities.

The average sizes of hybrid and crystalline cavities are similar in the late (mostly crystallized) structures of *run1* – 3. In *run0*, hybrid cavities are a third larger than crystalline, in *run2* they are one quarter larger, and in *run1* and *run3* they are of comparable size. In the early structures, the hybrid cavities are nearly twice as large as the amorphous or crystalline ones, and they are typically long multicavities with both types of neighbors.

Incomplete crystallization in *run1* – 3 leads to more cavities near amorphous atoms, and the relative number changes with changing crystallinity. Crystallization is most complete in *run2*, where the environment of nearly 400 Å^3 of cavities is crystalline, with slightly more than 400 Å^3 in a hybrid environment. For *run3*, the corresponding numbers are $\sim 200 \text{ Å}^3$ and nearly 400 Å^3 , although these values appear to converge to 275 Å^3 . At the end of *run1*, there are ~ 150

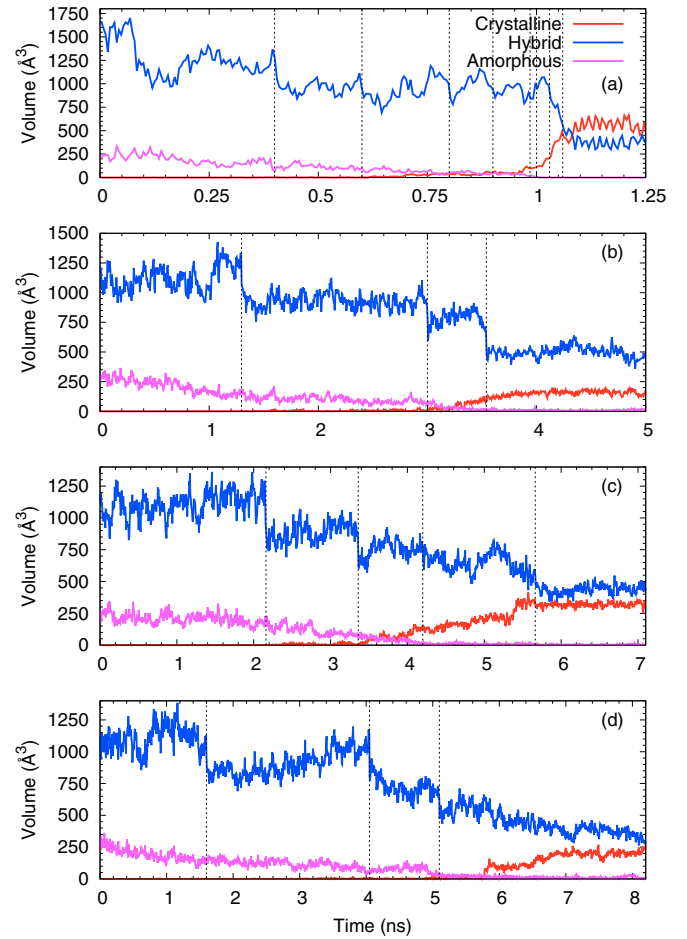


FIG. 7. Cavity volume breakdown by the local environment of the cavity. Crystalline and amorphous cavities have only crystalline or amorphous neighboring atoms as defined in the text. Hybrid cavities have both kinds or neighboring atoms. Panels (a)–(d) are *run0* – 3. Vertical dashed lines show changes in box size.

and $\sim 450 \text{ Å}^3$ of crystalline and hybrid cavities, respectively, reflecting the presence of grain boundaries.

D. Dynamical properties

The mean square displacements (MSD) of the atoms for *run1* – 3 are shown in Fig. 8. It is not surprising that the motion slows as crystallinity increases, and the enhanced mobility of Ge atoms in the supercooled liquid at 600 K has been noted previously [13]. The details of the mobility plots differ in the three simulations, emphasizing again the stochastic nature of the process. We note that Sb atoms are the most mobile in liquid GST at the melting point (900 K) [7] and in liquid $\text{Ge}_2\text{Sb}_8\text{Te}_{11}$ at 950 K [23].

The vibrational densities of states (vDOS) at the end of *run1* – 3 are shown in Fig. SF2 (supplemental material) [18]. The overall power spectra become narrower and move to lower frequencies as crystallization proceeds, as found previously in *run0* [14]. The high-frequency modes are related to Ge-Ge (“wrong”) bonds and tetrahedral Ge environments. Figure SF2 also shows the inverse participation ratios of the individual

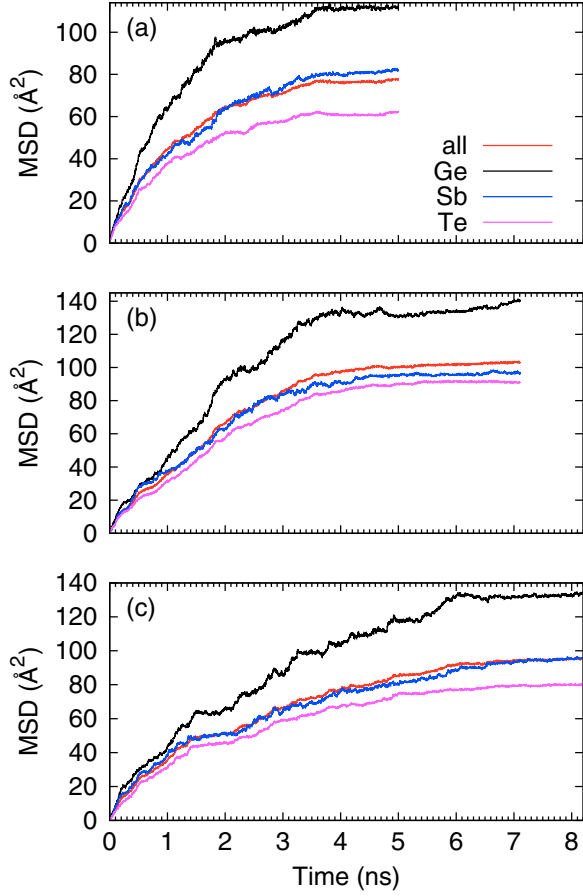


FIG. 8. Mean square displacement (MSD) atoms in (a) *run1*, (b) *run2*, and (c) *run3*.

vibration modes,

$$(\text{IPR})_j = \sum_{k=1}^N \left| \frac{\mathbf{e}(j,k)}{\sqrt{M_k}} \right|^4 / \left(\sum_{k=1}^N \frac{|\mathbf{e}(j,k)|^2}{M_k} \right)^2, \quad (1)$$

where $\mathbf{e}(j,k)$ is the eigenvector of mode j , and the sums run over atoms k with mass M_k . The IPR measures the spread of a state over the set of functions $\mathbf{e}(j,k)$ and is small if \mathbf{e} is spread across many atomic sites k . In the case of *run0* [14], localized vibration modes develop in the frequency range 15–25 cm^{-1} during crystallization, and this is also true in *run1* – 3. This appears to be a characteristic feature of crystallization in these materials. The localized, low-frequency ($<20 \text{ cm}^{-1}$) vibrations in *run1* have the largest amplitude in the region between the two clusters, and in *run2* and *run3* in the amorphous regions of the samples.

E. Electronic densities of states

Figure 9 shows the electronic density of states (eDOS) at the completion of *run1* – 3. The overall features are similar and can be characterized by a simple model used to discuss the differences between the eDOS in the amorphous and crystalline phases [7]. The π -band below the Fermi energy is derived from the 5*p* orbitals of Te and Sb, and the σ -band between -13 and -6 eV is derived from atomic *s*-components. The overlap between the bands is small. More details of the

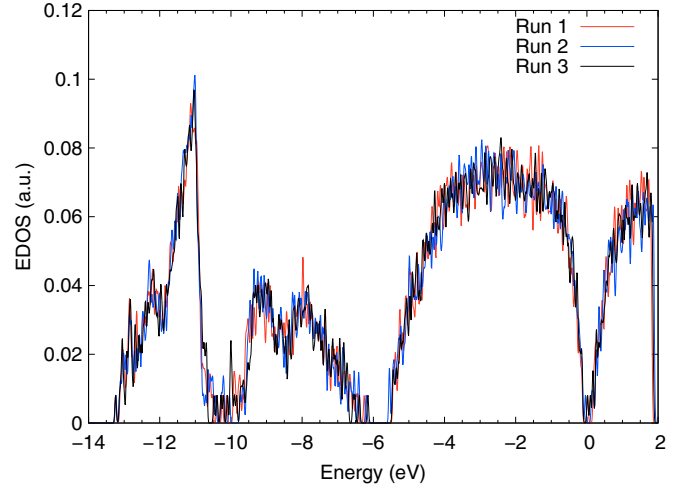


FIG. 9. Electronic densities of states (eDOS) at the end of *run1* – 3.

eDOS are provided in Fig. SF3 [18], which also shows the electronic inverse partition ratios, determined in analogy to Eq. (1) by projecting the Kohn-Sham orbitals onto a set of atomic functions. The band gap appears to be 0.2–0.3 eV, and there are several “impurity states.” It was shown recently how the optical gap in an amorphous semiconductor can be engineered using Hellmann-Feynman forces in conjunction with MD simulations [24].

The IPR, as in the case of vibrational modes, is a measure of the spatial localization of the states at a particular energy, and more details about the states in the immediate neighborhood of the Fermi energy are shown in Fig. SF4 [18]. In the case of *run3*, for example, the states in the band gap are localized in the remaining amorphous region and/or percolating across the crystallite in the x direction. In all three structures, the percolating states appear to avoid cavities.

IV. DISCUSSION

Crystallization occurred in simulations *run1* – 3, and both the process and the final structures differ markedly from earlier work on GST based on shorter simulations with fewer atoms. DF/MD simulations of GST (180 atoms, up to 400 ps, 600 K) [25,26] indicated that cavity diffusion to the crystal/glass interface, followed by Ge/Sb diffusion to these sites, resulted in cubic, cavity-free crystallites. There is no evidence for these effects here or in our earlier simulations [13]. The critical crystalline nucleus in these simulations (5–10 “ABAB cubes”) [25,26] is also smaller than we find here.

The arrangement of Ge, Sb, and cavities in *c*-GST has often been discussed [13], and substantial displacements from the ideal rocksalt positions may occur, particularly for Ge [11]. However, the model of a perfect Te sublattice is almost never questioned [2]. Energy optimization does appear to favor Te occupancy of one sublattice, but entropy speaks a different story. The nanosecond time scale will lead inevitably to one of the many structures with “wrong bonds,” rather than the relatively few with a perfect Te sublattice and slightly lower energy. The vibration frequencies in GST (typically

100 cm⁻¹ or 3 THz) [27] allow several thousand vibrations during crystallization, which allows significant atomic motion (including diffusion) in *all* elements, including Te [13].

The focus in the present work has been on the structural transformation between the amorphous and crystalline phases, but it is also of interest to comment on the initial and final structures in light of available experimental information. The differences between the x-ray photoelectron (XPS) spectra found in the amorphous and crystalline states [28] was reproduced well [7] by the differences between the electronic densities of states of the amorphous structure adopted here and a representative rocksalt structure of Yamada-type (perfect Te sublattice, random distribution of Ge, Sb, and vacancies on the other) [10]. The total XRD structure factor $S(Q)$ of amorphous GST [29] was reproduced reasonably well by this structure, and improved agreement was found by experimentally constrained density functional calculations [9]. Reverse Monte Carlo calculations often provide additional information, such as partial PDF g_{ij} , but RMC fits to the measured $S(Q)$ led without DF constraints to a metallic, rather than semiconducting, electronic structure [9].

The crystalline structures found in the present simulations have been compared with XRD [29] and ND [30] as follows [31]. From the atomic coordinates and the appropriate scattering weights for neutrons and x rays, we have determined the total pair distribution functions $G(r)$ [32]. The measured $S(Q)$ for XRD have been Fourier-transformed with a Q_{\max} of 20 Å⁻¹ and a Lorch modification function [33] to minimize truncation errors. The result is the experimental $G(r)$ for XRD,

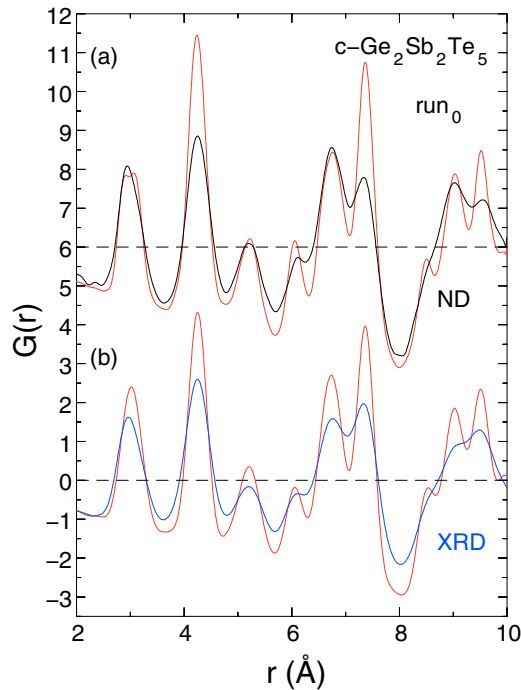


FIG. 10. Total pair distribution function $G(r)$. (a) Neutron diffraction (ND) data (Ref. [30], black) and present results (red), (b) x-ray diffraction (XRD) (Ref. [29], blue) and present results (red).

and the same procedure has been followed for the ND data ($Q_{\max} = 35$ Å⁻¹). It appears that Ref. [30] uses a different method for transforming the raw ND data, as some details of $G(r)$ differ from our results. We note that the Q_{\min} in these ND data is 1.67 Å⁻¹ [31], so that substantial truncation errors are to be expected.

The total neutron-weighted PDF $G(r)$ for a single crystalline structure of Yamada-type has been compared with the ND results [30] by Caravati *et al.* [3]. In Fig. 10, we compare the $G(r)$ calculated for our most stable crystalline structure (*run0*) with both ND and XRD results. The calculations reproduce the peak positions in $G(r)$ very well, but the oscillations are more pronounced than in experiment. By contrast, the oscillations in $G(r)$ in Ref. [3] are significantly weaker than in experiment, and the agreement with experiment is less satisfactory, particularly for $r \gtrsim 6.5$ Å.

The corresponding comparisons of the total PDF curves for the simulations described in the present work (*run1* – 3) are provided in the supplemental material [18], and they show generally better agreement with XRD data [29] than with ND [30]. The overall agreement is best for *run2*, the structure with the largest cluster of crystalline atoms (90% of total). The *run1* structure, with two crystalline clusters and the smallest cluster of crystalline atoms (59% of total), shows the least satisfactory agreement with experiment, particularly for larger values of r .

V. CONCLUDING REMARKS

The DF/MD simulations of crystallization of three amorphous 460-atom samples of GST at 600 K are by far the most extensive performed for this prototypical PC material. With 2–3 million self-consistent density functional calculations of each of three 460-atom samples, they are perhaps the most extensive DF calculations performed to date. The different densities of *a*- and *c*-GST (0.0308 and 0.0330 atoms/Å³, respectively) are accommodated by adjusting the cell size during the simulation. Crystallization is defined in terms of bond orientational order parameters, and we estimate the speed of crystallization to be ~ 0.7 – 0.9 m/s in *run0* and 0.3 – 0.4 m/s in *run1* – 3. We have focused on changes in the numbers of “*ABAB* squares” (*A*: Ge or Sb, *B*: Te), cavities, “wrong bonds,” and vibration frequencies. The correlation between the numbers of *ABAB* squares and crystalline atoms supports our early suggestion of the essential role played by these structural units [7,12], which can break and re-form during crystallization [13,26]. Nucleation and percolation in the early stages are important, and the latter, in particular, would be difficult to analyze with smaller simulation samples. Localized, low-frequency vibrational modes arise during the last stages of crystallization.

The presence of cavities in the amorphous and crystalline phases is characteristic of materials in the $(\text{GeTe})_{1-x}(\text{Sb}_2\text{Te}_3)_x$ family [34], and it is crucial to the rapid phase changes that occur. Cavity ordering occurs [14], and Ge and Sb atoms move *away* from cavities to occupy sites in one sublattice of the rocksalt structure. Growth of the crystal nucleus leads to connections with replicas in the neighboring cells (percolation) *before* the rapid stage of crystallization occurs. These findings caution against developing oversimplified models of

crystallization that focus on atomistic processes involving specific elements. A phase change that occurs on the nanosecond time scale at 600 K still allows diffusion and some thousands of vibrations, and all atoms are affected.

Three simulations at 600 K with the same starting structures, but different velocity distributions, show quite distinct crystallization behaviors. For example, *run1* showed the first clear signs of crystallization, but its final structure was the least crystalline (smallest clusters, fewest *ABAB* rings, highest energy). The stochastic nature of the phase change may warn against being surprised by this result, and it suggests that *many* more simulations are needed for a complete picture. A particularly interesting result is the presence of multiple crystallites in two of the three samples. In one case (*run1*), crystallization is favored in one crystallite over the other, while in another (*run3*) the formation of a grain boundary hampers further crystallization on the time scale accessible to

the present simulations. These findings are likely to be repeated in other simulations and other materials.

ACKNOWLEDGMENTS

We thank H. R. Schober for helpful discussions, S. Shamoto for providing the original ND data (Ref. [30]), and S. Kohara for providing the original XRD (Ref. [29]) and other data used in Fig. 10 and Figs. SF5–7. We gratefully acknowledge computer time provided by the JARA-HPC Vergabegremium on the JARA-HPC partition of the supercomputer JUQUEEN at Forschungszentrum Jülich, and for time granted on the supercomputers JUROPA and JURECA at Jülich Supercomputer Centre. Financial support was provided by the Academy of Finland through its Centres of Excellence Program (Project 284621) (J.A.) and the Singapore University of Technology and Design (J.K.).

-
- [1] G. W. Burr, M. J. Breitwisch, M. Franceschini, D. Garetto, K. Gopalakrishnan, B. Jackson, B. Kurdi, C. Lam, L. A. Lastras, A. Padilla, B. Rajendran, S. Raoux, and R. S. Shenoy, *J. Vac. Sci. Technol. B* **28**, 223 (2010).
 - [2] See, for example, S. Raoux, W. Welnic, and D. Ielmini, *Chem. Rev.* **110**, 240 (2010), and references therein.
 - [3] S. Caravati, M. Bernasconi, T. D. Kühne, M. Krack, and M. Parrinello, *J. Phys.: Condens. Matter* **21**, 255501 (2009).
 - [4] T. Matsunaga, J. Akola, S. Kohara, T. Honma, K. Kobayashi, E. Ikenaga, R. O. Jones, N. Yamada, M. Takata, and R. Kojima, *Nat. Mater.* **10**, 129 (2011).
 - [5] M. Schumacher, H. Weber, P. Jónvári, Y. Tsuchiya, T. G. A. Youngs, I. Kaban, and R. Mazzarello, *Sci. Rep.* **6**, 27434 (2016), and references therein (liquid GST).
 - [6] R. O. Jones, *Rev. Mod. Phys.* **87**, 897 (2015).
 - [7] J. Akola and R. O. Jones, *Phys. Rev. B* **76**, 235201 (2007).
 - [8] J. Akola and R. O. Jones, *Phys. Rev. Lett.* **100**, 205502 (2008).
 - [9] J. Akola, R. O. Jones, S. Kohara, S. Kimura, K. Kobayashi, M. Takata, T. Matsunaga, R. Kojima, and N. Yamada, *Phys. Rev. B* **80**, 020201(R) (2009).
 - [10] N. Yamada, *MRS Bull.* **21**, 48 (1996).
 - [11] N. Yamada and T. Matsunaga, *J. Appl. Phys.* **88**, 7020 (2000).
 - [12] J. Hegedüs and S. R. Elliott, *Nat. Mater.* **7**, 399 (2008).
 - [13] J. Kalikka, J. Akola, J. Larrucea, and R. O. Jones, *Phys. Rev. B* **86**, 144113 (2012).
 - [14] J. Kalikka, J. Akola, and R. O. Jones, *Phys. Rev. B* **90**, 184109 (2014).
 - [15] CPMD, version 3.15 <http://www.cpmc.org/>, ©IBM Corp 1990–2012, ©MPI für Festkörperforschung Stuttgart 1997–2001.
 - [16] P. J. Steinhardt, D. R. Nelson, and M. Ronchetti, *Phys. Rev. B* **28**, 784 (1983).
 - [17] I. Heimbach, F. Rhiem, F. Beule, D. Knodt, J. Heinen, and R. O. Jones (unpublished) (version 0.9.0). URL: <https://pgi-jcns.fz-juelich.de/portal/pages/pymoldyn-main.html>
 - [18] See supplemental material at <http://link.aps.org/supplemental/10.1103/PhysRevB.94.134105> for the final structures of *run1* – 3, which includes seven figures (Figs. SF1–7). SF1: view of final structure of *run1* along the *z*-axis and showing two crystallites; SF2: vibrational densities of states and inverse participation ratios (IPR); SF3: electronic densities of states and the corresponding IPR; SF4: an expanded view of SF3 in the neighborhood of the Fermi energy; SF5–7: comparison of experimental and calculated total pair distribution functions $G(r)$ (ND, XRD) for *run1* – 3.
 - [19] G. C. Sosso, G. Miceli, S. Caravati, F. Giberti, J. Behler, and M. Bernasconi, *J. Phys. Chem. Lett.* **4**, 4241 (2013).
 - [20] I. Ronneberger, W. Zhang, H. Eshet, and R. Mazzarello, *Adv. Funct. Mater.* **25**, 6407 (2015).
 - [21] J. Orava, A. L. Greer, B. Ghoulipour, D. W. Hewak, and C. E. Smith, *Nat. Mater.* **11**, 279 (2012).
 - [22] R. Jeyasingh, S. W. Fong, J. Lee, Z. Li, K.-W. Chang, D. Mantegazza, M. Asheghi, K. E. Goodson, and H.-S. P. Wong, *Nano Lett.* **14**, 3419 (2014).
 - [23] J. Akola and R. O. Jones, *Phys. Rev. B* **79**, 134118 (2009).
 - [24] K. Prasai, P. Biswas, and D. A. Drabold, *Semicond. Sci. Technol.* **31**, 073002 (2016).
 - [25] T. H. Lee and S. R. Elliott, *Phys. Rev. B* **84**, 094124 (2011).
 - [26] T. H. Lee and S. R. Elliott, *Phys. Rev. Lett.* **107**, 145702 (2011).
 - [27] J. Akola and R. O. Jones, *J. Phys.: Condens. Matter* **20**, 465103 (2008).
 - [28] J.-J. Kim, K. Kobayashi, E. Ikenaga, M. Kobata, S. Ueda, T. Matsunaga, K. Kifune, R. Kojima, and N. Yamada, *Phys. Rev. B* **76**, 115124 (2007).
 - [29] S. Kohara, K. Kato, S. Kimura, H. Tanaka, T. Usuki, K. Suzuya, H. Tanaka, Y. Moritomo, T. Matsunaga, N. Yamada, Y. Tanaka, H. Suematsu, and M. Takata, *Appl. Phys. Lett.* **89**, 201910 (2006).
 - [30] S. Shamoto, K. Kodama, S. Iikubo, T. Taguchi, N. Yamada, and T. Proffen, *Jpn. J. Appl. Phys.* **45**, 8789 (2006).
 - [31] S. Kohara (private communication).
 - [32] D. A. Keen, *J. Appl. Crystallogr.* **34**, 172 (2001).
 - [33] E. Lorch, *J. Phys. C* **2**, 229 (1968).
 - [34] T. Matsunaga, R. Kojima, N. Yamada, K. Kifune, Y. Kubota, Y. Tabata, and M. Takata, *Inorg. Chem.* **45**, 2235 (2006).